JACS
JOURNAL OF THE AMERICAN CHEMICAL SOCIETY
Article
pubs.acs.org/JACS

Protein Structural Dynamics of Photoactive Yellow Protein in Solution Revealed by Pump–Probe X-ray Solution Scattering

Tae Wu Kim,[†,∥] Jae Hyuk Lee,[†,∥] Jungkweon Choi,[†,∥] Kyung Hwan Kim,[†] Luuk J. van Wilderen,[‡] Laurent Guerin,[§,⊥] Youngmin Kim,[†] Yang Ouk Jung,[†] Cheolhee Yang,[†] Jeongho Kim,[†] Michael Wulff,[§] Jasper J. van Thor,*[,‡] and Hyotcherl Ihee*[,†]

[†]Center for Time-Resolved Diffraction, Department of Chemistry, Graduate School of Nanoscience & Technology (WCU), KAIST, Daejeon, 305-701, Republic of Korea

[‡]Division of Molecular Biosciences, Imperial College London, South Kensington Campus, SW7 2AZ London, United Kingdom

[§]European Synchrotron Radiation Facility, Grenoble Cedex 9, France

Supporting Information

ABSTRACT: Photoreceptor proteins play crucial roles in receiving light stimuli that give rise to the responses required for biological function. However, structural characterization of conformational transition of the photoreceptors has been elusive in their native aqueous environment, even for a prototype photoreceptor, photoactive yellow protein (PYP). We employ pump–probe X-ray solution scattering to probe the structural changes that occur during the photocycle of PYP in a wide time range from 3.16 μs to 300 ms. By the analysis of both kinetics and structures of the intermediates, the structural progression of the protein in the solution phase is vividly visualized. We identify four structurally distinct intermediates and their associated five time constants and reconstructed the molecular shapes of the four intermediates from time-independent, species-associated difference scattering curves. The reconstructed structures of the intermediates show the large conformational changes such as the protrusion of N-terminus, which is restricted in the crystalline phase due to the crystal contact and thus could not be clearly observed by X-ray crystallography. The protrusion of the N-terminus and the protein volume gradually increase with the progress of the photocycle and becomes maximal in the final intermediate, which is proposed to be the signaling state. The data not only reveal that a common kinetic mechanism is applicable to both the crystalline and the solution phases, but also provide direct evidence for how the sample environment influences structural dynamics and the reaction rates of the PYP photocycle.

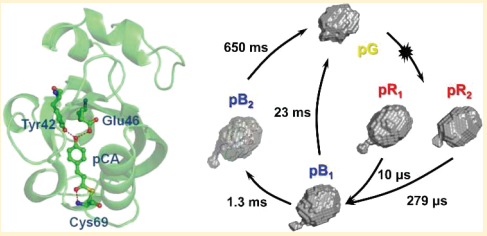

INTRODUCTION

In all kingdoms of life and functions, light is often used as an input signal to initiate structural and chemical processes via photoreception. Photoactive yellow protein (PYP) is a small photoreceptor protein that is presumably involved in the negative phototaxis of the bacterium Halorhodospira halophila and has served as a model system for understanding the photoreception and the subsequent signal transduction at a molecular level. Accordingly, PYP has been the focus of many experimental and computational studies aimed at resolving the structural and spectroscopic characteristics of reaction intermediates formed in its photocycle.[1−21] Its chromophore, 4-hydroxycinnamic acid (or *p*-coumaric acid, pCA), is bound to Cys69 through a thioester linkage (Figure 1).[21] A photocycle is triggered upon blue excitation of the "pG" ground state (λ_{max} = 446 nm) and accompanies structural changes that are spectroscopically characterized with multiple time constants ranging from ultrafast[12,17,22,23] to millisecond and subsecond time scales.[2,9,15,16,20,24,25] The pCA chromophore of the photoexcited pG state undergoes trans-to-cis isomerization, and the first intermediate, denoted I_0, is formed on picosecond time scale.[17,22,23] Consequently, thermally activated processes occur on nano-, micro-, and millisecond time scales, accompanying the formation of red-shifted (pR; λ_{max} = 465 nm) and blue-shifted (pB; λ_{max} = 355 nm) intermediates.

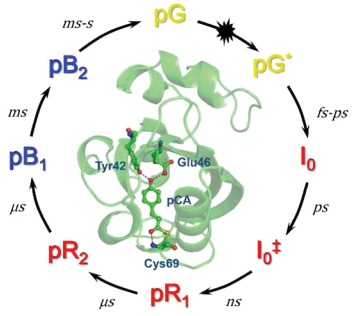

Figure 1. General photocycle of photoactive yellow protein with corresponding time region. On illumination with the visible light, the ground state is induced to photoreaction pathway with the isomerization of chromophore region.

Received: November 7, 2011
Published: February 3, 2012

Understanding the protein structural dynamics of PYP photocycle requires not only the characteristic reaction rates but also detailed molecular structures of all of the intermediates involved in the photocycle. To reveal the structures of transient intermediates, many different techniques have been applied. Small-angle X-ray scattering (SAXS), which is able to provide the global structural information of proteins including the radius of gyration and molecular shape,[13,14,26−37] revealed that the light-induced signaling state of PYP accompanies the increase of protein volume and the decrease of secondary structure content as compared to the ground state.[13,14] However, in these studies, only mutants or truncated PYP were used to slow the photocycle and accumulate specific intermediates, and therefore the overall kinetics and conformational dynamics of wild-type PYP were not examined. Time-resolved X-ray crystallography,[5,38−42] which effectively probes short-lived dynamical structures with high spatial and temporal resolutions, was also applied to probe the structural dynamics of PYP.[5] Although a comprehensive reaction mechanism was proposed on the basis of time-resolved electron densities, it is believed that the three-dimensional structure of the late intermediate (called I_2' or pB_2) in crystal is different from the structure in solution due to crystal contacts resulting in restricted structural change.[5,6,16] Time-resolved spectroscopic studies of PYP in both solution and crystalline phases suggested that the reaction pathways strongly depend on the sample phase, proposing that the reaction pathways visualized by time-resolved X-ray crystallography may not represent the common kinetic framework applicable to the solution phase.[1,43,44] As another means of probing the transient structures of PYP photocycle, NMR spectroscopy was applied and elucidated the structural details and equilibrium fluctuations for the pB_2 intermediate,[8,18,19,45] but did not provide adequate information for intermediates formed at the earlier stage of the photocycle due to limited time resolution of NMR spectroscopy. Thus, despite these numerous efforts, currently there is no consensus on the operational kinetic mechanism and protein conformational change during PYP photocycle.

In this situation, pump−probe X-ray solution scattering[46−52] is a great alternative because this method provides direct structural information with superb time resolution and can be easily applied to physiological aqueous phase. In other words, using the pump−probe X-ray solution scattering, it is possible to collect time-dependent structural information for the early structural precursors as well as the long-lived pB_2 signaling state in the solution phase. Here, we use pump−probe X-ray solution scattering to study detailed structural dynamics of the PYP photocycle in a wide time range from 3.16 μs to 300 ms. The data analysis shows four structurally distinct intermediates (pR_1, pR_2, pB_1, and pB_2) and their associated time constants. We reconstruct the molecular shapes of these four intermediates from time-independent species-associated difference scattering curves extracted from quantitative kinetic analysis. The reconstructed shape of the pB_2 state extracted only from X-ray scattering data measured in this study is consistent with the structure refined using combined data from DEER, NMR, and X-ray scattering measurements,[6] confirming the integrity of molecular structure extracted from X-ray scattering data alone. Our results on both kinetics and structures of the intermediates clearly visualize the structural dynamics of PYP photocycle and provide a unified kinetic framework for the PYP photocycle.

EXPERIMENTAL SECTION

Data Acquisition. Time-resolved X-ray solution scattering data were collected at the beamline ID09B of ESRF, while the storage ring was operated in the 16-bunch mode at 6 GeV. Protocols for data collection and data processing have been reported in detail elsewhere.[50] A 4.4 mM PYP solution in a Na-phosphate buffer with 20 mM NaCl at pH 7 was mounted in a quartz capillary with 1 mm diameter (Hampton Research). The capillary was mounted in a goniometer so that its axis is perpendicular to the propagation directions of the laser and X-ray pulses, which are also perpendicular to each other. To initiate a photoreaction, we used the laser pulses at 460 nm where the extinction coefficient of the sample is 34 200 M^{-1} cm^{-1}. Nanosecond laser pulses at 460 nm were generated from a solid-state nanosecond laser (Vibrant, Opotek) utilizing an OPO setup pumped by a Nd:YAG laser. The laser beam was sent to the sample vertically (from above to down) and was focused to an elliptical spot of 1.28 × 0.5 mm^2 at the top part of the capillary, and the energy density was 1 mJ/mm^2. Polychromatic (3.5% bandwidth) X-ray pulses peaked at 18 keV in 16-bunch mode were sent to the sample in a direction perpendicular to both the capillary axis and the laser excitation, and the scattered X-rays were collected in a CCD detector (MarCCD). Solution scattering was measured over a wide q range ($q = 4\pi \sin(\theta)/\lambda$, where 2θ is the scattering angle and λ is the X-ray wavelength) from 0.04138 to 2.0891 $Å^{-1}$. To reduce the scattering from the air, a cone filled with helium gas was used between the sample and the MarCCD. The X-ray spot size at the sample was 0.06 × 0.1 mm^2, and its position at the sample was 150 μm from the top surface of the capillary. The data collection was done at a repetition rate of 5 Hz typically, and to ensure a fully recovered ground-state population for each laser shot, the capillary was translated by 0.2 mm after each probe pulse. The laser-off images were acquired with laser pulses arriving 50 μs earlier than the X-ray pulse to probe the ground state while assuring the same average temperature of the solution. These laser-off images were used to compute the time-resolved X-ray scattering differences. Usually, a laser-off image was collected after every three or four laser-on images to compensate for slow drifts of X-ray intensity in the beamline. The measured time delays are spread evenly in logarithmic time scale and are as follows: −50 μs, 3.16 μs, 5.62 μs, 10 μs, 17.8 μs, 31.6 μs, 56.2 μs, 100 μs, 178 μs, 316 μs, 562 μs, 1 ms, 1.78 ms, 3.16 ms, 5.62 ms, 10 ms, 17.8 ms, 31.6 ms, 56.2 ms, 100 ms, 200 ms, and 300 ms. These delays cover the time range for conversion of the pR state into the pB state and the subsequent partial decay of the pB state back to the pG ground state. The data at −50 μs contain structural information of the pG ground state, while the data at positive time delays contain the contributions from a mixture of ground state and photoproducts. Pump-on minus pump-off difference scattering curves were generated by subtracting the data at −50 μs, which brings out the change caused by photoexcitation and can be modeled by photoproducts minus the ground state. A total of 100 images were collected for each time delay and averaged to provide a sufficient signal-to-noise ratio. Two-dimensional images were converted to one-dimensional curve, $I(q)$, as a function of momentum transfer q according to the established protocol.[50]

Kinetic Analysis Using Singular Value Decomposition and Principal Component Analysis. To examine the number of kinetic components and their relaxation times, we applied the singular value decomposition (SVD) to the experimental data in the q range of 0.04138−1.0 $Å^{-1}$. The relaxation times were determined by simultaneously fitting the four principal time-dependent components (right singular vectors) with a sum of five exponentials sharing common relaxation times. These relaxation times were used in the subsequent principal component analysis (PCA) based on a kinetic model (sequential or parallel). In PCA, the theoretical time-resolved difference scattering curve at each time delay is generated as a linear combination of the species-associated difference scattering curves obeying the kinetics determined by the kinetic model. By minimizing the discrepancy between the experimental and theoretical time-resolved difference scattering curves, the species-associated scattering

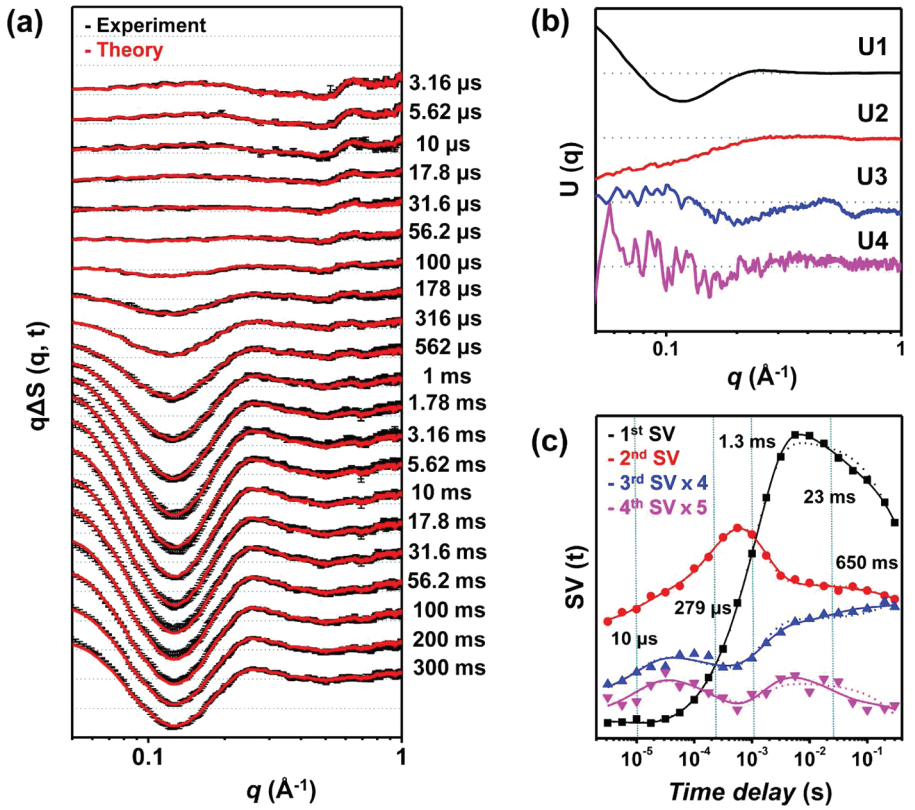

Figure 2. Time-resolved X-ray solution scattering data of the PYP photocycle and singular value decomposition (SVD) analysis. (a) The black curves are experimental difference curves ($\Delta S(q, t) = S(q, t) - S(q, -50\ \mu s)$) obtained by subtracting the scattering curve at −50 μs from the curves at other time delays. The red curves are theoretical data obtained from principal component analysis. Here, the theoretical data are a linear sum of species-associated difference scattering curves obeying a kinetic model shown in Figure 3A. The full kinetic data set with delays from 3.16 μs to 300 ms, over a q range from 0.0414 to 1.0 Å^{-1}, plotted with logarithmic q axes. (b) The most significant left-singular vectors (U). (c) The most significant right-singular vectors (V) multiplied by corresponding singular values (S). The solid lines are fitted to each SV by using five exponential functions with the following time constants: 10 μs, 279 μs, 1.3 ms, 23 ms, and 650 ms. The dotted line is the fit without the 23 ms component, giving worse agreement.

curves for four intermediates were extracted and used for further shape reconstruction. The details are shown in the Supporting Information.

Scaling of Experimental Difference Curves To Construct Species-Associated Scattering Curves. For shape reconstruction using DAMMIN, the static scattering curve for each intermediate species is constructed by adding a theoretical static scattering curve for pG calculated using CRYSOL[53] to the scaled species-associated difference scattering curve. As an input to the calculation of the theoretical scattering curve for pG, we used the coordinates of the ensemble averaged structure, 3PHY pdb[19] derived from NMR. We note that the theoretical curve calculated from 3PHY well reproduces the experimental static scattering curve, as shown in Supporting Information Figure 4. The scale factor depends on both the photolyzed fraction and the experiment-to-theory scale factor. The full photoconversion is expected (see the Supporting Information for the details). The experiment-to-theory scale factor was obtained by comparing the experimental scattering curve at −50 μs with the theoretical curve from 3PHY.

Previously, SAXS measurements were conducted on a truncated mutant of PYP lacking the first six amino acids under stoichiometric photoconversion with intense continuous illumination and showed that the radius of gyration (R_g) obtained from Guinier plot analysis increases by 1.1 Å for this mutant.[14] We thus constructed a scattering curve for the pure pB species by limiting R_g to be approximately 1 Å larger than the ground state, as described in the Supporting Information. Using this procedure, the extrapolated zero-intensity (I_0), which is related to the solvent-excluded volume, was found to increase by 4.2% relative to the ground state, in agreement with the scale factor estimated from the power density. Table 2 shows the values of R_g and I_0 for each intermediate (see the Supporting Information for the details).

Molecular Shape Reconstruction from Species-Associated Scattering Curves. From the species-specific static scattering curves, R_g and the radial distribution function (RDF), $P(r)$, were calculated for each intermediate by indirect Fourier transformation using the GNOM program.[54] When extracting a RDF from a species-associated static curve, the maximum dimension (D_{max}), which is an input parameter for GNOM, plays a critical role in describing the RDFs appropriately. To acquire reasonable input values for D_{max}, we first calculated the size of protein from R_g because R_g is directly related to the radius of protein under the assumption that the protein is of spherical or ellipsoidal shape. Actually, the input value of D_{max} to GNOM was set to be 20% larger than the estimated value from R_g because an underextimated D_{max} value might constrain the shape reconstruction. This upper limit of D_{max} is reasonable based on the study of M100L mutant, which shows a light-induced increase of R_g by 5% relative to the ground state.[13] On the other hand, because indirect transformation is used to calculate the RDFs, excessively large (>50%) value of D_{max} causes a large error in the calculation of RDFs. Using optimal RDFs and species-associated static curves, simulated annealing calculations from 0.04138 to 0.6 Å^{-1} were implemented to refine the intermediate structures with DAMMIN package.[55] For each species-specific curve, multiple runs of calculation were performed to make a structure pool reflecting structural fluctuation. From this structure pool containing 40−50 reconstructed structures, the representative reconstructed structure was generated to represent an average structure of each intermediate (see the Supporting Information for details). To generate the represented structure, all reconstructed

dx.doi.org/10.1021/ja210435n | J. Am. Chem. Soc. 2012, 134, 3145−3153

Table 1. Comparison of Time Constants Determined from Previous Studies of PYP Photocycle Using Various Techniques

	TA[a]	FT-IR[b]	TR-ORD[c]	TG[d]	TR-Laue[e]	This Work[f]
$pR_1 \rightarrow pR_2$ ($pR_1 \rightarrow pB_1$)[g]	1 μs		10 μs	1 μs	(30 μs)	(10 μs)
$pR_2 \rightarrow pB_1$	260 μs	113 μs		170 μs	333 μs	279 μs
$pB_1 \rightarrow pB_2$	1.5 ms	1.5 ms	1.5 ms	1 ms	18 ms	1.3 ms
$pB_1 \rightarrow pG$					10 ms	23 ms
$pB_2 \rightarrow pG$	360 ms	189 ms, 583 ms	515 ms	ms−s	141 ms	650 ms

[a]Transient Absorption Spectroscopy (ref. 1). [b]Time-Resolved Fourier-Transform Infrared Spectroscopy (ref. 2). [c]Time-Resolved Optical Rotatory Dispersion Spectroscopy (ref. 3). [d]Transient Grating Spectroscopy (ref. 4). [e]Time-Resolved Laue X-ray Crystallography (ref. 5). [f]Pump-Probe X-ray Solution Scattering (Liquidography). [g]The assignment depends on the reaction model. The numbers in parenthesis are from the parallel model and the others are from the sequential model.

structures from DAMMIN are superimposed to a template structure (or reference structure) using DAMSEL and DAMSUP. Next, the well-aligned structures were overlapped to make a probability map, which reflects the maximum displacement of each intermediate using DAMAVER.[56] Finally, using DAMFILT, we filtered a representative structure that has high densities on the probability map. In addition to DAMMIN, we also used GASBOR to reconstruct the shape. Due to high constraint to maintain the folded structure in the default GASBOR parameters, the tail of the experimental RDF was not reproduced in the theoretical RDF.

RESULTS

Figure 2a shows the difference scattering curves, $\Delta S(q,t)$, obtained by subtracting the reference scattering curve measured at −50 μs from the scattering curves at various positive time delays. Strong signals at small q values (<0.3 Å^{-1}) start to build from early microsecond time scales and become increasingly prominent at later time delays. Along with the strong features in the small q-region, oscillatory features are observed at large q values (>0.45 Å^{-1}), corresponding to structural features of high spatial resolution (see the Supporting Information for the details).

Quantitative kinetic analysis was conducted by using singular value decomposition (SVD) to determine the rate constants that describe the time-dependent change of the entire data set (see the Supporting Information for the details). The first four principal time-independent components (left singular vectors) shown in Figure 2b exhibit features of small amplitude in high q region in addition to the major oscillation features. The first four principal time-dependent components (right singular vectors) scaled with singular values from the SVD analysis on the data in the q range of 0.04138−1.0016 Å^{-1} were simultaneously fit with a sum of five exponentials, yielding the time constants of 10 μs (±2.5 μs), 280 μs (±18 μs), 1.3 ms (±0.05 ms), 23 ms (±6 ms), and 650 ms (Figure 2c). Among these, the 23 ms component occurs on a time scale similar to the response arising from solvent heating. However, when fitting without the 23 ms component, the fit quality substantially deteriorates in the 10−300 ms time range, indicating that the 23 ms component is required to fit the entire data.

To account for the kinetic components (four intermediates and five time constants) determined from the SVD analysis of the pump−probe X-ray solution scattering data, we considered two candidate kinetic models: parallel (Figure 4b) and sequential (Figure 4d) kinetic pathways. In the parallel model, two types of pR intermediates (pR_1 and pR_2) are formed simultaneously and convert to pB_1 intermediate at different rates. In contrast, pR_1 and pR_2 are sequentially formed in the sequential model. The parallel model was determined to be an effective kinetic mechanism in the crystalline PYP by time-resolved X-ray crystallography,[5] while the sequential model has been commonly used in the spectroscopic studies of PYP[1,4,16] (Table 1). In Table 1, the time constants determined from previous studies of PYP photocycle using various techniques are listed and compared with the result from this work. We note that pump-probe solution scattering in this work captured all the kinetic components that were detected by other methods, while some of the components are missing in other works. Considering that spectroscopy and X-ray scattering are sensitive to the environment around the chromophore and the entire protein, respectively, the common kinetic components in the results from the various techniques suggests that the structural change in the chromophore region is highly correlated with the global conformational change during the photocycle of PYP.

On the basis of both parallel and sequential kinetic models, we performed principal component analysis (PCA) using the time constants determined from the SVD analysis (see the Supporting Information for the details). From the PCA analysis, species-associated difference scattering curves for the four intermediates (pR_1, pR_2, pB_1, and pB_2) were extracted as shown in Figure 3a (parallel) and c (sequential). The experimental scattering curves at all time delays can be represented by a linear combination of those species-associated scattering curves. The amplitude change of the time-independent species-associated scattering curves corresponds to the population kinetics of the reaction intermediate species, as shown in Figure 3b (parallel) and d (sequential). The intermediates identified with distinct time constants from our analysis represent structurally distinct intermediates that are uniquely identified by X-ray scattering (Table 1).

To have more detailed information on the intermediate structures, we performed the reconstruction of the molecular shapes from the species-associated scattering curves. To do so, we employed the dynamical annealing procedure of pseudo atoms using DAMMIN program.[55] Figure 4a and c shows the surface plots of the reconstructed structures based on the parallel and sequential kinetic model, respectively, together with the time constants associated with each step of the photocycle. The reconstructed shapes and the molecular parameters for the intermediates (listed in Table 2) are different between the two kinetic models.

Because the protein concentration is high and the salt concentration is rather low, the structure factor due to the interparticle interactions may play a role. According to in-depth studies on the correlation of the structure factor and the sample concentration for bovine serum albumin[57] and ovalbumin,[58] the contribution of the structure factor is significant for the

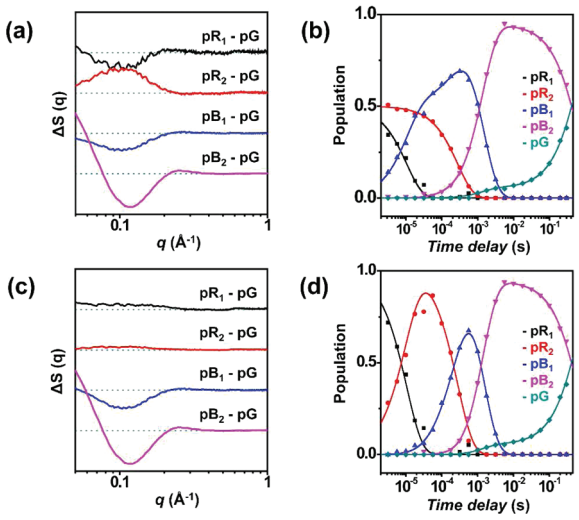

Figure 3. Time-independent species-associated difference scattering curves for the intermediates and populations change. (a) Species-associated difference scattering curves for the parallel model (Figure 4a) are extracted from PCA analysis. (b) Population change for the parallel model. (c) Species-associated difference scattering curves for the sequential model (Figure 4b) are extracted from the same procedure used for the parallel model. (d) Population change for the sequential model. The solid lines in (b) and (d) represent theoretical population changes compatible with the kinetic models, and the symbols in (b) and (d) are from fitting experimental curve at each time delay with a sum of species-associated scattering curves.

scattering intensity at q less than 0.04 Å^{-1}. Because our shape reconstruction uses the data at q larger than 0.042 Å^{-1}, we do not expect that the structure factor greatly affects the reconstructed shapes. However, the interparticle interactions can be protein specific, and thus further studies with various protein and salt concentrations are needed to completely rule out the effect of the structure factor in our analysis.

DISCUSSION

Reconstructed Structures of Intermediates. From the species-associated scattering curves obtained from PCA, we can obtain detailed structural change of the intermediate species involved in the PYP photocycle. For example, the species-associated difference scattering curve for pB_2 (Figure 3a and c) exhibits increased scattering intensity at small q values and reduced scattering intensity around q = 0.13 Å^{-1} as compared to the pG state. In general, this type of species-associated difference scattering curve is indicative of increased radius of gyration (R_g) and increased maximum diameter (D_{max}).

According to the structural analysis, the three-dimensional reconstructed shape of each intermediate gives an insight to the structural transition of PYP photocycle. First, as can be seen in Figure 4, one end of the protein protrudes in pR_1 and pR_2 and the protrusion gradually becomes more prominent with the progress of the photocycle, becoming maximal in pB_2. The reconstructed shape of pB_1 (alternatively called I_2 state[9]), which is the structural precursor of the fully developed signaling state pB_2 (also called I_2'[9] or pB[5]), shows a smaller degree of protrusion than does pB_2. The protrusion observed in all of the intermediates is likely to be the N-terminus region, which has been known to be perturbed in the pB_2 state.[5,6,45] As the reconstructed shape of pB_2 is superimposed on the signaling structure (PDB code 2KX6) determined from DEER, NMR, and X-ray scattering,[6] it can be seen that both the direction and the extent of the protrusion well match the N-terminus region (Figure 4b and d), confirming the assignment of the protrusion to the N-terminus of PYP.

The shape reconstruction employed in this work essentially uses the low structural resolution information contained at rather small angles (q < 0.3 Å^{-1}). The higher-resolution information in the higher q range does not contribute much to the shape reconstruction, and the reconstructed shapes cannot provide any higher-resolution insight. Therefore, it is desirable to develop a structural analysis tool that incorporates the high-resolution information.

The structural parameters of the intermediates (Table 2) provide insights that connect the findings from previous studies using various techniques. In particular, the extracted radii of gyration for the intermediates show that the volume of the protein gradually expands. The transition from pR_2 to pB_1 causes a considerable change of protein volume with respect to pG state. The volume of pB_2 state is about 18% larger than that of pG. This volume expansion may be linked to the structural change around the chromophore-binding pocket as proposed by a FTIR study.[16] In that study, it was suggested that the opening of the chromophore-binding pocket is driven by intramolecular proton transfer between pCA and Glu46. The volume expansion is also consistent with the crystal structure of the intermediates determined by time-resolved X-ray crystallography, which characterizes the structural change around pCA chromophore explicitly.[5] Whereas pR_{CW} and pR_{E46Q}, which respectively correspond to pR_1 and pR_2, sustain hydrogen bonds between pCA and neighbor residues such as Tyr42 and Glu46, these hydrogen bonds are broken in the pB_2 state by the structural reorientation of the chromophore, thereby allowing the pB_2 structure to expand.

Parallel versus Sequential Model. The kinetic components determined from pump–probe X-ray scattering curves (Figure 4a) are remarkably consistent with those derived from the time-resolved X-ray crystallography measurement of PYP crystals in the P_6^3 space group (Figure 4b).[5] In that study, the red-shifted pR intermediate was determined to be of heterogeneous nature with two types of pR states (pR_1 and pR_2) existing together, indicating that the parallel model is the working mechanism in the crystalline phase. The coexistence of the two pR states was also reported in a study using resonance Raman spectroscopy.[10] In the crystalline phase, the pR_1 and pR_2 states convert to the blue-shifted pB_1 intermediate with 30 and 333 μs time constants, respectively.[5] Subsequently, the pB_1 intermediate either returns directly to pG with 10 ms time constant or converts to the final intermediate pB_2 with 18 ms time constant. Finally, pB_2 decays to the pG ground state with 140 ms time constant.

However, we note that the sequential model, where pR_1, pR_2, and pB_1 are formed sequentially ($pR_1 \rightarrow pR_2 \rightarrow pB_1$), fits the pump–probe X-ray scattering data to the same quality as the parallel model. This is a typical uncertainty problem in kinetics and, to favor one model over the other, arguments other than the quality of the global fitting are required. To address this issue, we consider the information available from time-resolved X-ray crystallography together with the solution scattering data and provide the following arguments favoring the parallel model over the sequential model.

First, we note that the microsecond kinetic component, which was assigned to the $pR_1 \rightarrow pR_2$ transition in the sequential model (Table 1), appears as a very weak signal in the

dx.doi.org/10.1021/ja210435n | J. Am. Chem. Soc. 2012, 134, 3145–3153

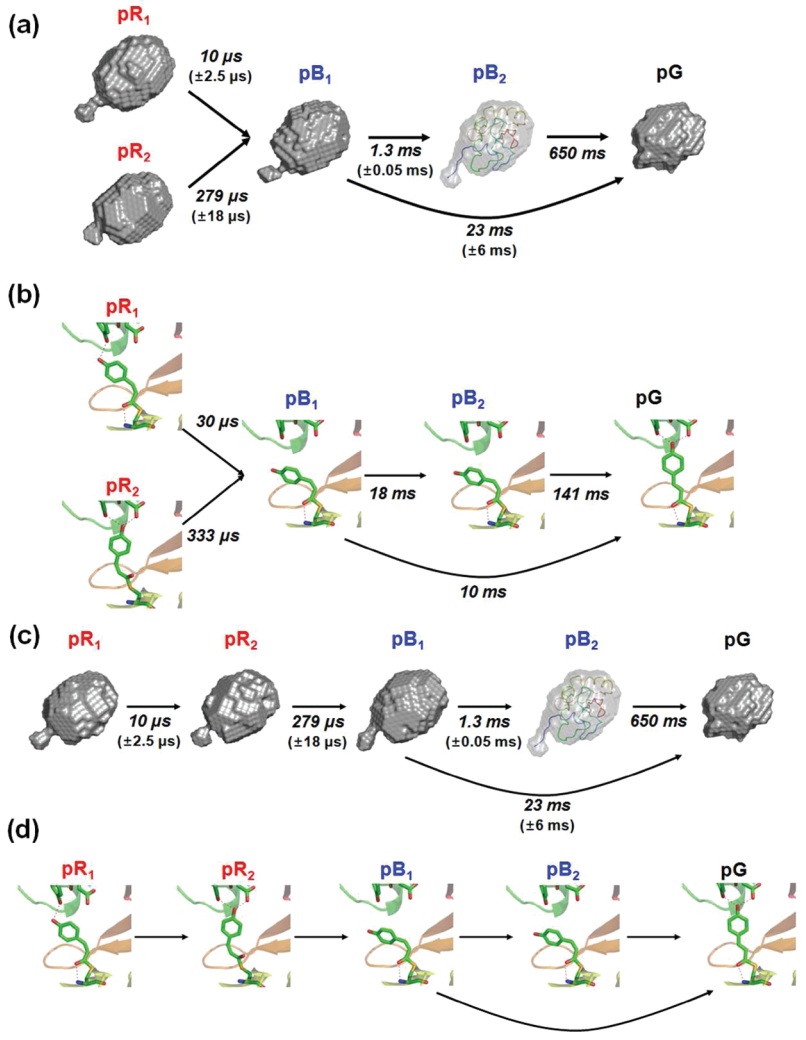

Figure 4. Structural dynamics of PYP photocycle revealed by pump−probe X-ray solution scattering. (a) Reconstructed molecular shapes of the intermediates and their associated time constants for the parallel model. (b) The time constants in the crystalline phase determined by time-resolved X-ray crystallography[5] are shown for comparison, together with the chromophore structure and its hydrogen bonds to the neighboring residues. (c) Reconstructed molecular shapes of the intermediates and their associated time constants for the sequential model. (d) The chromophore structures determined from time-resolved crystallography are rearranged according to the sequential model. In this case, the benzene ring has to reorient opposite directions twice ($pR_1 \rightarrow pR_2$ and $pR_2 \rightarrow pB_1$), involving multiple hydrogen-bond breaking and making. Regardless of the kinetic model, the protrusion is maximized for pB_2, which is assumed to be the signaling state. The reconstructed structures of pB_2 from the parallel model (gray surface) and the sequential model (gray surface) are superimposed on the one (rainbow cartoon) from the study combining DEER, NMR, and SAXS/WAXS experiment (PDB: 2KX6).[6] The reconstructed shapes perfectly cover the pB_2 structure revealed by the combined structural probes, including the direction of elongated N-terminus.

Table 2. Structural Parameters Including Radius of Gyration (R_g), Maximum Distance (D_{max}), and Zero Intensity (I_0) for Each Intermediate in Each Kinetic Model and Ground State (3PHY)

	sequential model			parallel model		
	R_g (Å)	D_{max} (Å)	I_0	R_g (Å)	D_{max} (Å)	I_0
pR_1	15.13	52.22	4.128×10^7	15.4	57.47	4.156×10^7
pR_2	15.07	51.17	4.113×10^7	14.88	48.09	4.102×10^7
pB_1	15.31	55.07	4.140×10^7	15.26	53.83	4.124×10^7
pB_2	15.68	58.09	4.258×10^7	15.68	58.09	4.258×10^7
pG	14.83	41.02	4.086×10^7	14.83	41.02	4.086×10^7

visible transient absorption measurement[1,20] and is not observed at all by infrared spectroscopy[2,16] although a significant change in the orientation and hydrogen bonds of the chromophore is expected if the sequential model were operational. The same argument holds even if pR_1 and pR_2 are exchanged in order in the sequential model. In contrast, in the parallel model, the same component of microsecond time constant is assigned to the $pR_1 \rightarrow pB_1$ transition. In pR_1 and pB_1, the orientation of the chromophore and the surrounding hydrogen-bond network stay similar, and thus the $pR_1 \rightarrow pB_1$ transition is likely to give a small signal in the visible transient absorption and infrared absorption measurements. Thus, the

dx.doi.org/10.1021/ja210435n | J. Am. Chem. Soc. 2012, 134, 3145−3153

microsecond kinetic component observed in our time-resolved solution scattering and other measurements in the literature is more consistent with the parallel model and can be assigned to $pR_1 \rightarrow pB_1$.

Second, the sequential model ($pR_1 \rightarrow pR_2 \rightarrow pB_1$) would involve unrealistic "back-and-forth" reorientation of the phenolic ring and alternate formation and breakage of the hydrogen bonds of the chromophore (Figure 4d). Thus, we consider that this scenario is highly unlikely. By contrast, the parallel model does not involve such unlikely back-and-forth reorientation of the chromophore.

Third, the molecular shapes of the intermediates in the parallel model show a correlation with the phenol ring orientation and the hydrogen bonding around the chromophore of the relevant intermediates determined from time-resolved Laue crystallography. In contrast, such correlation is not found in the case of the sequential model. The species-associated curve constructed for each intermediate species can be used to determine the molecular shape, the radial distribution function (RDF), and the radius of gyration R_g (Table 2). In the parallel model, the protrusion of the N-terminus of pR_2 is much less than that of the other intermediates (pR_1, pB_1, and pB_2). According to the structures determined by time-resolved Laue crystallography, only the pR_2 maintains the hydrogen bond with Glu46, and consequently the phenol ring orients toward Glu46, whereas this hydrogen bond is broken in the other intermediates and thus the phenol ring orients away from Glu46. In the sequential model, pR_1 and pR_2 show similar degrees of protrusion, and such correlation is not found. Because the molecular shape determines the scattering curve, this correlation is also seen in the species-associated difference scattering curves. In the parallel model, the species-associated difference curve for pR_2 has positive intensity around $q = 0.1$ Å^{-1}, whereas those for the other intermediates have negative intensity (Figure 3a). The sequential model does not show such correlation (Figure 3c).

Fourth, the parallel model can account for both time-resolved X-ray crystallography data and time-resolved solution scattering data, whereas the sequential model accounts for only the solution scattering data. Time-resolved X-ray crystallography has the power to discriminate the kinetic models as the atomic-resolution structures are visualized in the time-dependent electron density maps. For example, when assuming the sequential kinetic model, the pR intermediate is clearly a mixture of two structures, while the parallel kinetic model provides two intermediates formed in parallel. Although the structural dynamics in the crystalline state may restrict large conformational changes observed in the pB states, it is unlikely that the crystal contact affects the kinetics of the pR intermediates where the structural changes are confined mostly to the chromophore region.

From all of the arguments described above, we suggest that the parallel kinetic mechanism should be operational in both the solution and the crystalline phases.

Insights to Kinetics and Structural Transition. From the parallel kinetic model that is applicable to both the crystalline and the solution phases, we can observe a profound effect of the sample environment on the dynamics of the PYP photocycle. The time constants (10 μs, 280 μs, and 23 ms) for $pR_1 \rightarrow pB_1$, $pR_2 \rightarrow pB_1$, and $pB_1 \rightarrow pG$ in the solution phase (Figure 4a) are comparable to the corresponding ones (30 μs, 333 μs, and 18 ms) in the crystalline phase (Figure 4b). However, the $pB_1 \rightarrow pB_2$ transition is accelerated by 14 times in the solution phase (1.3 ms) than in the crystalline phase (18 ms). As shown in the reconstructed shapes, the formation of pB_2 accompanies the largest structural change involving the protrusion of N-terminus. Therefore, the transition of $pB_1 \rightarrow pB_2$ can be highly restricted in the crystalline phase unlike in the solution phase. The faster recovery of pB_2 to pG in the crystalline phase (141 ms) than in the solution phase (650 ms) is also consistent with the effect of the crystalline contact.

The global molecular shapes of the intermediates clearly visualize the N-terminus protrusion in pR_1, pB_1, and pB_2. Such protrusion was not clearly observed in the crystalline phase by time-resolved Laue crystallography, except that a very small movement of the N-terminus was observed for pB_2 even in the crystalline phase.[5] This contrast in the N-terminus movement between the solution and crystalline phases provides direct evidence that the crystalline contact restricts such large conformational changes.

The parallel model in combination with the structures of intermediates from time-resolved Laue crystallography provides important insight to how the global protein conformation is coupled to the hydrogen bond between the Glu46 and the phenol ring of the chromophore. pR_2 maintains the hydrogen bonds to Tyr42 and Glu46 residues. As a result, the overall protein structure of pR_2 in the solution phase is likely to stay compact and thus have small R_g and D_{max} values, in agreement with the parallel model rather than the sequential model (Table 2). By contrast, the hydrogen bond to Glu46 is broken in the other intermediates. The phenol ring in pR_1 has only the hydrogen bond to Tyr42, and that in pB_1 and pB_2 has no hydrogen bond. One plausible hypothesis inferred from this observation is that the hydrogen bond to Glu46 plays an important role in maintaining the entire protein structure, and thus its absence may cause the entire protein to undergo structural transformation of large amplitude.

■ CONCLUSION

The kinetics and structural dynamics of the photocycle of PYP were investigated by pump−probe X-ray solution scattering for a wide time range of 3.16 μs to 300 ms. Kinetic analysis establishes four structurally distinct intermediates (pR_1, pR_2, pB_1, and pB_2) and five time constants (10 μs, 280 μs, 1.3 ms, 23 ms, and 650 ms), regardless of the reaction mechanism. Our results elucidate the molecular shapes of the intermediates formed in the PYP photocycle and suggest that a common kinetic mechanism involving parallel formation and decay of two pR species may be operational in both the solution and the crystalline phases. However, the global molecular shape and the reaction rate of the intermediate accompanying large conformational change in the solution phase show dramatic difference from those in the crystalline phase that were determined by time-resolved X-ray Laue crystallography. The protrusion of the N-terminus and the protein volume increase as the photocycle progresses and are maximized in the last intermediate (pB_2). This study is the first instance where the three-dimensional molecular envelopes of the protein intermediates are reconstructed with microsecond time resolution and should serve as a cornerstone for further structural studies of protein structural dynamics in solution phase.

■ ASSOCIATED CONTENT

Supporting Information

Figures, tables, and materials. This material is available free of charge via the Internet at http://pubs.acs.org.

AUTHOR INFORMATION

Corresponding Author

hyotcherl.ihee@kaist.ac.kr; j.vanthor@imperial.ac.uk

Present Address

[⊥]Institut de Physique de Rennes, Université de Rennes1-CNRS, UMR 6251, 35042 Rennes, France.

Author Contributions

[∥]These authors contributed equally.

ACKNOWLEDGMENTS

We thank Marco Cammarata for his help in the data collection. This work was supported by Creative Research Initiatives (Center for Time-Resolved Diffraction) of MEST/NRF. We acknowledge the support from the WCU program (R31-2008-000-10071-0). J.J.v.T. is supported by the European Research Council via Grant Agreement No. 208650.

REFERENCES

(1) Yeremenko, S.; van Stokkum, I. H. M.; Moffat, K.; Hellingwerf, K. J. *Biophys. J.* **2006**, *90*, 4224.

(2) Brudler, R.; Rammelsberg, R.; Woo, T. T.; Getzoff, E. D.; Gerwert, K. *Nat. Struct. Biol.* **2001**, *8*, 265.

(3) Chen, E.; Gensch, T.; Gross, A. B.; Hendriks, J.; Hellingwerf, K. J.; Kliger, D. S. *Biochemistry* **2003**, *42*, 2062.

(4) Terazima, M.; Hoshihara, Y.; Imamoto, Y.; Kataoka, M.; Tokunaga, F. *Biophys. J.* **2008**, *94*, 2187.

(5) Ihee, H.; Rajagopal, S.; Srajer, V.; Pahl, R.; Anderson, S.; Schmidt, M.; Schotte, F.; Anfinrud, P. A.; Wulff, M.; Moffat, K. *Proc. Natl. Acad. Sci. U.S.A.* **2005**, *102*, 7145.

(6) Ramachandran, P. L.; Lovett, J. E.; Carl, P. J.; Cammarata, M.; Lee, J. H.; Jung, Y. O.; Ihee, H.; Timmel, C. R.; van Thor, J. J. *J. Am. Chem. Soc.* **2011**, *133*, 9395.

(7) van Stokkum, I. H.; Gobets, B.; Gensch, T.; Mourik, F.; Hellingwerf, K. J.; Grondelle, R.; Kennis, J. T. *Photochem. Photobiol.* **2006**, *82*, 380.

(8) Vreede, J.; Crielaard, W.; Hellingwerf, K. J.; Bolhuis, P. G. *Biophys. J.* **2005**, *88*, 3525.

(9) Joshi, C. P.; Borucki, B.; Otto, H.; Meyer, T. E.; Cusanovich, M. A.; Heyn, M. P. *Biochemistry* **2005**, *44*, 656.

(10) Unno, M.; Kumauchi, M.; Hamada, N.; Tokunaga, F.; Yamauchi, S. *J. Biol. Chem.* **2004**, *279*, 23855.

(11) Itoh, K.; Sasai, M. *Chem. Phys.* **2004**, *307*, 121.

(12) Groot, M. L.; van Wilderen, L. J.; Larsen, D. S.; van der Horst, M. A.; van Stokkum, I. H.; Hellingwerf, K. J.; van Grondelle, R. *Biochemistry* **2003**, *42*, 10054.

(13) Sasaki, J.; Kumauchi, M.; Hamada, N.; Oka, T.; Tokunaga, F. *Biochemistry* **2002**, *41*, 1915.

(14) Imamoto, Y.; Kamikubo, H.; Harigai, M.; Shimizu, N.; Kataoka, M. *Biochemistry* **2002**, *41*, 13595.

(15) Hendriks, J.; Gensch, T.; Hviid, L.; van Der Horst, M. A.; Hellingwerf, K. J.; van Thor, J. J. *Biophys. J.* **2002**, *82*, 1632.

(16) Xie, A.; Kelemen, L.; Hendriks, J.; White, B. J.; Hellingwerf, K. J.; Hoff, W. D. *Biochemistry* **2001**, *40*, 1510.

(17) Ujj, L.; Devanathan, S.; Meyer, T. E.; Cusanovich, M. A.; Tollin, G.; Atkinson, G. H. *Biophys. J.* **1998**, *75*, 406.

(18) Rubinstenn, G.; Vuister, G. W.; Mulder, F. A.; Dux, P. E.; Boelens, R.; Hellingwerf, K. J.; Kaptein, R. *Nat. Struct. Biol.* **1998**, *5*, 568.

(19) Dux, P.; Rubinstenn, G.; Vuister, G. W.; Boelens, R.; Mulder, F. A.; Hard, K.; Hoff, W. D.; Kroon, A. R.; Crielaard, W.; Hellingwerf, K. J.; Kaptein, R. *Biochemistry* **1998**, *37*, 12689.

(20) Hoff, W. D.; van Stokkum, I. H.; van Ramesdonk, H. J.; van Brederode, M. E.; Brouwer, A. M.; Fitch, J. C.; Meyer, T. E.; van Grondelle, R.; Hellingwerf, K. J. *Biophys. J.* **1994**, *67*, 1691.

(21) Hoff, W. D.; Dux, P.; Hard, K.; Devreese, B.; Nugteren-Roodzant, I. M.; Crielaard, W.; Boelens, R.; Kaptein, R.; van Beeumen, J.; Hellingwerf, K. J. *Biochemistry* **1994**, *33*, 13959.

(22) Kennis, J. T.; Groot, M. L. *Curr. Opin. Struct. Biol.* **2007**, *17*, 623.

(23) Larsen, D. S.; van Stokkum, I. H.; Vengris, M.; van Der Horst, M. A.; de Weerd, F. L.; Hellingwerf, K. J.; van Grondelle, R. *Biophys. J.* **2004**, *87*, 1858.

(24) Hendriks, J.; Hellingwerf, K. J. *J. Biol. Chem.* **2009**, *284*, 5277.

(25) Takeshita, K.; Imamoto, Y.; Kataoka, M.; Mihara, K.; Tokunaga, F.; Terazima, M. *Biophys. J.* **2002**, *83*, 1567.

(26) Konuma, T.; Kimura, T.; Matsumoto, S.; Got, Y.; Fujisawa, T.; Fersht, A. R.; Takahashi, S. *J. Mol. Biol.* **2011**, *405*, 1284.

(27) Kathuria, S. V.; Guo, L.; Graceffa, R.; Barrea, R.; Nobrega, R. P.; Matthews, C. R.; Irving, T. C.; Bilsel, O. *Biopolymers* **2011**, *95*, 550.

(28) Roux, B.; Yang, S. C.; Blachowicz, L.; Makowski, L. *Proc. Natl. Acad. Sci. U.S.A.* **2010**, *107*, 15757.

(29) Roh, J. H.; Guo, L.; Kilburn, J. D.; Briber, R. M.; Irving, T.; Woodson, S. A. *J. Am. Chem. Soc.* **2010**, *132*, 10148.

(30) Zuo, X.; Wang, J.; Foster, T. R.; Schwieters, C. D.; Tiede, D. M.; Butcher, S. E.; Wang, Y. *J. Am. Chem. Soc.* **2008**, *130*, 3292.

(31) Forster, F.; Webb, B.; Krukenberg, K. A.; Tsuruta, H.; Agard, D. A.; Sali, A. *J. Mol. Biol.* **2008**, *382*, 1089.

(32) Akiyama, S.; Takahashi, S.; Kimura, T.; Ishimori, K.; Morishima, I.; Nishikawa, Y.; Fujisawa, T. *Proc. Natl. Acad. Sci. U.S.A.* **2002**, *99*, 1329.

(33) Doniach, S. *Chem. Rev.* **2001**, *101*, 1763.

(34) Hura, G. L.; Menon, A. L.; Hammel, M.; Rambo, R. P.; Poole, F. L.; Tsutakawa, S. E.; Jenney, F. E.; Classen, S.; Frankel, K. A.; Hopkins, R. C.; Yang, S. J.; Scott, J. W.; Dillard, B. D.; Adams, M. W. W.; Tainer, J. A. *Nat. Methods* **2009**, *6*, 606.

(35) Tsuruta, H.; Irving, T. *Curr. Opin. Struct. Biol.* **2008**, *18*, 601.

(36) Lamb, J. S.; Zoltowski, B. D.; Pabit, S. A.; Crane, B. R.; Pollack, L. *J. Am. Chem. Soc.* **2008**, *130*, 12226.

(37) Koch, M. H. J.; Vachette, P.; Svergun, D. I. *Q. Rev. Biophys.* **2003**, *36*, 147.

(38) Knapp, J. E.; Pahl, R.; Cohen, J.; Nichols, J. C.; Schulten, K.; Gibson, Q. H.; Srajer, V.; Royer, W. E. Jr. *Structure* **2009**, *17*, 1494.

(39) Schotte, F.; Lim, M. H.; Jackson, T. A.; Smirnov, A. V.; Soman, J.; Olson, J. S.; Phillips, G. N.; Wulff, M.; Anfinrud, P. A. *Science* **2003**, *300*, 1944.

(40) Bourgeois, D.; Vallone, B.; Schotte, F.; Arcovito, A.; Miele, A. E.; Sciara, G.; Wulff, M.; Anfinrud, P.; Brunori, M. *Proc. Natl. Acad. Sci. U.S.A.* **2003**, *100*, 8704.

(41) Moffat, K. *Chem. Rev.* **2001**, *101*, 1569.

(42) Srajer, V.; Teng, T.; Ursby, T.; Pradervand, C.; Ren, Z.; Adachi, S.; Schildkamp, W.; Bourgeois, D.; Wulff, M.; Moffat, K. *Science* **1996**, *274*, 1726.

(43) Kort, R.; Ravelli, R. B.; Schotte, F.; Bourgeois, D.; Crielaard, W.; Hellingwerf, K. J.; Wulff, M. *Photochem. Photobiol.* **2003**, *78*, 131.

(44) Ng, K.; Getzoff, E. D.; Moffat, K. *Biochemistry* **1995**, *34*, 879.

(45) Bernard, C.; Houben, K.; Derix, N. M.; Marks, D.; van der Horst, M. A.; Hellingwerf, K. J.; Boelens, R.; Kaptein, R.; van Nuland, N. A. *Structure* **2005**, *13*, 953.

(46) Kim, K. H.; Oang, K. Y.; Kim, J.; Lee, J. H.; Kim, Y.; Ihee, H. *Chem. Commun.* **2011**, *47*, 289.

(47) Kim, J.; Kim, K. H.; Kim, J. G.; Kim, T. W.; Kim, Y.; Ihee, H. *J. Phys. Chem. Lett.* **2011**, *2*, 350.

(48) Cho, H. S.; Dashdorj, N.; Schotte, F.; Graber, T.; Henning, R.; Anfinrud, P. *Proc. Natl. Acad. Sci. U.S.A.* **2010**, *107*, 7281.

(49) Kim, T. K.; Lee, J. H.; Wulff, M.; Kong, Q.; Ihee, H. *ChemPhysChem* **2009**, *10*, 2915.

(50) Cammarata, M.; Levantino, M.; Schotte, F.; Anfinrud, P. A.; Ewald, F.; Choi, J.; Cupane, A.; Wulff, M.; Ihee, H. *Nat. Methods* **2008**, *5*, 881.

(51) Ihee, H.; Lorenc, M.; Kim, T. K.; Kong, Q. Y.; Cammarata, M.; Lee, J. H.; Bratos, S.; Wulff, M. *Science* **2005**, *309*, 1223.

(52) Ihee, H. *Acc. Chem. Res.* **2009**, *42*, 356.

(53) Svergun, D. I.; Barberato, C.; Koch, M. H. J. *J. Appl. Crystallogr.* **1995**, *28*, 768.

(54) Svergun, D. I. *J. Appl. Crystallogr.* **1992**, *25*, 495.
(55) Svergun, D. I. *Biophys. J.* **1999**, *76*, 2879.
(56) Volkov, V. V.; Svergun, D. I. *J. Appl. Crystallogr.* **2003**, *36*, 860.
(57) Zhang, F. J.; Skoda, M. W. A.; Jacobs, R. M. J.; Martin, R. A.; Martin, C. M.; Schreiber, F. *J. Phys. Chem. B* **2007**, *111*, 251.
(58) Ianeselli, L.; Zhang, F. J.; Skoda, M. W. A.; Jacobs, R. M. J.; Martin, R. A.; Callow, S.; Prevost, S.; Schreiber, F. *J. Phys. Chem. B* **2010**, *114*, 3776.